1993ApJ...414..510S

THE ASTROPHYSICAL JOURNAL, 414:510–526, 1993 September 10
© 1993. The American Astronomical Society. All rights reserved. Printed in U.S.A.

SHOCK EXCITATION OF THE EMISSION-LINE FILAMENTS IN CENTAURUS A

RALPH S. SUTHERLAND, GEOFFREY V. BICKNELL, AND MICHAEL A. DOPITA
Mount Stromlo and Siding Spring Observatories, Australian National University,
Private Bag, Weston Creek Post Office, ACT 2611, Australia
Received 1992 November 10; accepted 1993 March 12

ABSTRACT

We present a self-consistent model for the excitation of the extranuclear emission line filaments in Centaurus A. Interaction of the northern radio jet of Centaurus A with a dense cloud of material at the location of the filaments causes shock waves with velocities $\sim$200–450 km s^{-1}. The shocks produce a strong flux of EUV and soft X-ray radiation which photoionize the visible knots.

We show that the mechanical flux of a mildly supersonic low-density jet is sufficient to energize the shock waves through the production of supersonic turbulent velocities in the dense cloud via the Kelvin-Helmholtz instability. Furthermore, the expected instability growth time scales, turbulent velocities, and characteristic wavelengths are all in agreement with the observations.

Detailed models of cloud-cloud collisions, using the new MAPPINGS II shock and photoionization code, produce a very good fit to the observed spectra when allowance is made for shock instabilities and cloud-cloud density contrasts. The high-excitation and low-excitation forbidden lines are reproduced along with the Hβ luminosity and temperature-sensitive [O III] λ4363/(5007+4959) ratio.

We predict the presence of a radio jet in the vicinity of the inner filaments and the presence of strong ultraviolet line fluxes in the spectrum of the filaments. The latter prediction is in contrast to the beamed photoionization models.

We conclude that a narrow ionizing radiation beam is not required to produce the observed phenomena. Moreover, many properties of the knots, such as the velocity field, are deduced in the model presented here whereas they are ad hoc assumptions in a simple beamed radiation model. Similar models involving shocks with velocities $\gtrsim$200 km s^{-1} may also be relevant to the extended and nuclear line emission from a wide variety of active galaxies.

Subject headings: galaxies: individual (NGC 5128) — galaxies: jets — galaxies: kinematics and dynamics — radiation mechanisms: miscellaneous — shock waves

1. INTRODUCTION

The emission-line filaments of Centaurus A were discovered independently by Blanco et al. (1975) and Peterson, Dickens, & Cannon (1975), and since that time, their interpretation has presented an interesting challenge to observers and theoreticians. Graham & Price (1981) obtained spectra of a number of the filaments and showed that the filaments exhibit a large velocity dispersion—a fact which is fundamental to a correct interpretation if the theory presented in this paper contains an element of truth. All of these workers also showed that the spectra display unusually high [O III] emission, beyond the range observed in normal H II regions and slow fully radiative shocks, and this is one of the key observational characteristics which a successful theory is required to explain.

More recent and more detailed observations, in the form of narrow-band imaging and high- and low-dispersion spectra, of the "inner" and "outer" filaments in Centaurus A have been obtained by Morganti et al. (1991). These workers recovered the result of Graham & Price, that the filaments have a high velocity dispersion and to some extent, mapped this out, finding sharp changes in velocities ranging from 200 to 400 km s^{-1} as well as line-splitting of the same order of magnitude in some regions. They also showed that the spectra contained a significant flux in low-excitation lines such as [O I] λ6300 and the [S II] $\lambda\lambda$6717+31 in addition to the high-excitation lines previously mentioned. On the basis of their data Morganti et al. (1991) have argued that the filaments are photoionized by an EUV–X-ray continuum which is beamed from the galaxy core, thereby suggesting that Centaurus A is a blazar viewed at such an angle that we do not directly see the highly beamed continuum emission. Morganti et al. (1991) show that the beaming in their model is not brought about by obscuration of the core by, say a dusty torus, since the obscured radiation would be reradiated in the infrared and the required infrared flux is not observed. Thus the required beaming presumably corresponds to relativistic beaming in a UV–X-ray continuum. In a subsequent paper Morganti et al. (1992) show that there is an ionization gradient in the "inner filaments" and argue that the direction of the ionization gradient supports their model.

The images obtained by Morganti and coworkers of both the inner and outer filaments show that the two sets of filaments are quite different morphologically. The inner filaments are fairly linear whereas the outer filaments are laterally extended and show several interesting arclike features. The morphological features of the outer filaments prompted simulations by Bicknell (1991) of transverse supersonic streams interacting with stationary dense material. Arclike features strikingly similar to some of the regions in the outer filaments were reproduced in these simulations. Since interactions of a dense gas with a transonic stream seem to be implicated in at least some of the morphological features of the filaments, Bicknell (1991) argued that the excitation of the filaments is also due to such an interaction. Binette, Dopita, & Tuohy (1985) had, in the context of AGN emission, suggested that high-velocity shocks could produce a sufficient flux of ionizing

© American Astronomical Society • Provided by the NASA Astrophysics Data System

radiation to ionize precursor material. Bicknell (1991) adapted this idea in a model for the Centaurus A filaments which showed that autoionizing shocks are feasible on energy grounds and which also estimated the correct Balmer-line flux for the observed velocity dispersion for the most prominent knots.

Thus, there are two qualitatively quite different ideas for these filaments, and the major purpose of this paper is develop further and in detail the autoionizing shock model. However, we should also emphasize that the correct interpretation of the Centaurus A data has ramifications well beyond this particular case. First, the concept of beaming plays a significant rôle in various *unification schemes*, and it is important to ascertain the usefulness and limits of the unified approach. Second, as Morganti et al. have noted, the line ratios of the filaments are typical of the line ratios in many radio galaxy extended emission-line regions, possibly indicating a common excitation mechanism. Third, there are other important examples of apparent jet–emission-line region interactions in radio galaxies such as Coma A (van Breugel et al. 1985) and Seyfert galaxies (Whittle 1989). The physical processes may well be similar to those occurring in Centaurus A.

The plan of this paper is as follows: In § 2 we elaborate upon the calculations presented in Bicknell (1991) and show that the production of the emission-line luminosity of the inner filaments is energetically consistent with the interaction of dense clouds with a jet whose parameters (Mach number and density ratio) are consistent with our knowledge of the parameters of jets in Fanaroff-Riley class I radio sources. We also demonstrate that the turbulent velocities observed in the filaments are consistent with their production by the Kelvin-Helmholtz instability acting at the jet-cloud interface. Order of magnitude estimates for the luminosity of the brightest knots in the inner Centaurus A filaments are derived and consistency between the observed velocity dispersion and the Hβ luminosity of the knots is demonstrated. In §§ 3 and 4 we present detailed model calculations of UV- and X-ray–emitting shocks using the latest, extended, version of the MAPPINGS photoionization and shock code (Sutherland 1993). In these sections we work through a succession of models ultimately presenting what we believe to be the most successful model for the emission-line regions—that of the collision of two unequal density clouds with relative velocities of the order of 300 km s^{-1}. Such a collision gives rise to a fast shock and a slow shock. The former produces the flux of UV and soft X-ray radiation which photoionizes the surrounding gas producing the high-excitation component of the spectrum, and the latter is primarily responsible for the low-excitation lines. Our best model provides good estimates for all of the optically observed lines, including the temperature-sensitive line [O III] λ4363 as well as making useful predictions for the fluxes of various UV lines. The UV fluxes are quite distinct from those predicted by the beaming model. The sizes of the line-emitting regions are correctly estimated.

2. BASIC PHYSICS AND ORDER OF MAGNITUDE ESTIMATES

2.1. *Outline of Model*

In outline, our model for the emission line luminosity is as follows: Interaction of dense molecular clouds with the outflowing plasma in the radio source (velocity ~1000–10,000 km s^{-1}) produces, through the Kelvin-Helmholtz instability, a turbulent supersonic velocity field in the gas which is being ablated from the dense cloud. Clumps of supersonically moving material collide with each other and produce strong shocks which radiate a large fraction of their internal energy in a flux of UV–soft X-ray photons. These photons irradiate the precursor gas, producing a high-excitation photoionized spectrum. The low-excitation part of the spectrum arises from shock waves in the dense gas.

This model is motivated by two important observed properties of the filaments. First, they are located near the so-called middle lobe of Centaurus A. The Morganti et al. outer filaments are located in the southern part of this lobe, whereas the inner filaments are located between the "middle lobe" and "inner lobe" along the direction of the inner northern jet. The unpublished radio images which form the basis of these comments (Burns 1991) are of low dynamic range, and there is no jet visible at the location of the inner filaments. However, the second major property of the filaments, their high internal velocity dispersion ($\gtrsim$200 km s^{-1}), first remarked upon by Graham & Price (1981) and studied in detail by Morganti et al. (1991) and Morganti et al. (1992), suggests that the filaments are interacting strongly with rapidly moving plasma. An additional feature of the more recent data is the line splitting ~200–400 km s^{-1} in some regions.

In any case, the existence of a jet at the location of the inner filaments is an important qualitative prediction of this model. Furthermore, the different locations of the inner and outer filaments (with respect to lobe and jet) qualitatively explains their different morphology: Clouds interacting with a supersonic/transonic collimated jet will be more elongated by the flow than clouds interacting with the flow in a subsonic lobe.

2.2. *The Energy Budget*

In this subsection we consider the energy budget of our model and show that the energy flux incident upon the filaments is capable of powering the emission lines.

Here and in the following sections we concentrate on the inner filaments since it is for those that the highest quality data are available.

It is generally accepted that the velocities of nonthermal plasma in class I extragalactic radio sources such as Centaurus A are at most mildly supersonic (e.g., Bicknell et al. 1990b). It is also reasonable to assume that regions such as the inner lobes contain material which is still in motion at approximately transonic speeds (cf. the simulations of Norman, Burns, Sulkanen 1988). Thus the jet energy flux intercepted by each of the knots in the inner filaments is

$$\begin{aligned} F_E &= \frac{\gamma}{\gamma - 1} P_{\rm jet} A_{\rm knot} v_{\rm jet} \left(1 + \frac{\gamma - 1}{2} M_{\rm jet}^2\right) \\ &= 1.0 \times 10^{37} \frac{\gamma_{\rm jet}^{3/2}}{\gamma_{\rm jet} - 1} \eta^{-1/2} \\ &\quad \times \left(\frac{n_{\rm ism}}{10^{-3}}\right)\left(\frac{T_{\rm ism}}{10^7}\right)^{3/2} \eta^{-1/2} \left(\frac{A}{10^4 {\rm pc}^2}\right) \\ &\quad \times M_{\rm jet}\left(1 + \frac{\gamma_{\rm jet} - 1}{2} M_{\rm jet}^2\right) {\rm ergs\ s}^{-1} , \end{aligned} \tag{1}$$

where $M_{\rm jet}$ is the jet Mach number and η is the ratio of the lobe density to the density of the hot interstellar medium. (See, for example, Bicknell 1986 for the source of expressions for the jet energy flux.) Some of the fiducial parameters in the above

TABLE 1

JET VELOCITIES AND ENERGY BUDGET

γ	$T_{\rm ism}/10^7$ K	$\mathcal{M}$	η	$V_{\rm jet}$ (10^3 km s^{-1})	F_E (10^{38} ergs s^{-1})
5/3	1.0	1.0	1.0	0.5	1.7
5/3	1.0	2.0	1.0	1.0	3.4
4/3	1.0	1.0	0.1	4.3	6.8
4/3	1.0	1.5	0.1	6.5	10.2
4/3	1.0	2.0	0.1	8.6	13.6
4/3	1.0	2.0	0.2	4.3	9.6
4/3	1.0	2.0	0.5	1.7	6.1
5/3	2.0	1.0	1.0	0.7	4.9
5/3	2.0	2.0	1.0	1.4	9.7
4/3	2.0	1.0	0.1	6.1	19.3
4/3	2.0	1.5	0.1	9.2	28.9
4/3	2.0	2.0	0.1	12.2	38.6
4/3	2.0	2.0	0.2	6.1	27.3
4/3	2.0	2.0	0.5	2.4	17.2
5/3	3.0	1.0	1.0	0.8	8.9
5/3	3.0	2.0	1.0	1.7	17.9
4/3	3.0	1.0	0.1	7.5	35.4
4/3	3.0	1.5	0.1	11.2	53.1
4/3	3.0	2.0	0.1	15.0	70.8
4/3	3.0	2.0	0.2	7.5	50.1
4/3	3.0	2.0	0.5	3.0	31.7

expression are obtained from Burns, Feigelson, & Schreier (1983) who estimate a number density $n_{\rm ism} \approx 3 \times 10^{-3}$ cm^{-3} in the region $3' < r < 6'$ from the galaxy center. Using their density profile $n(r) \propto r^{-1.8}$ and assuming that the gas density is $\approx 3 \times 10^{-3}$ at $r = 4'.5$ implies that the gas density at the radius of the inner filaments is $\sim 10^{-3}$ cm^{-3}. Fabian et al. (1986) estimate $T_{\rm ism} \approx 1.4 \times 10^7$ K using a derived temperature-luminosity relation for elliptical galaxies. The [O III] images of Morganti et al. (1991) show that the projected cross sections of the clouds are $\approx 4 \times 10^4$ pc^2. If the jet is not substantially mixed with the ISM then, most likely $\gamma \approx 4/3$ and $\eta < 1$. If substantial mixing has occurred, then $\gamma = 5/3$ and $\eta \approx 1$.

With our proposed mechanism, virtually all of the incident energy flux is dissipated by the shocks produced by cloud-cloud collisions. As we show below, most of the postshock internal energy is radiated, and for optical depths $\gtrsim 1$ most of the above energy flux is reradiated in line emission. For a normally photoionized H II region the total line flux is about 50 times the Hβ flux. In the photoionization scenario we are discussing here, this factor may exceed 100 (see following section). Since the Hβ flux is approximately $\sim 10^{37}$ ergs s^{-1} for each of the bright knots A, B, and C, approximately 10^{39} ergs s^{-1} of incident energy are required. In Table 1 we show the incident energy fluxes calculated for a plausible range of jet parameters and for $n_{\rm ism} = 10^{-3}$ cm^{-3} and $A_{\rm knot} = 4 \times 10^4$ pc^2. (The energy flux scales directly with these parameters.)

One can see from this table that the energy requirements are met by quite reasonable jet parameters, generally Mach numbers in the range of 1–2 and density ratios in the range of 0.1–1.0. The energy requirements are slightly easier to meet when $T_{\rm ism} > 10^7$. However, we regard the fact that we can easily get to within an order of magnitude of the required value to be a compelling argument in favor of the basic model. The velocities implied by these jet parameters are also given in Table 1. The velocities most consistent with the energy budget are in the range of 2000–10,000 km s^{-1} and are in accordance with what we normally expect for jet velocities in class I sources.

2.3. *Development of a Supersonic Turbulent Region through the Kelvin-Helmholtz Inability*

2.3.1. *Magnitude of the Induced Velocity*

As we stated above, we suggest that the Kelvin-Helmholtz instability is most likely involved in the production of supersonic turbulence within the dense cloud. The contour maps of the [O III] images support this idea. The morphology they reveal (the contour maps are not dominated by the brightest regions of emission as are the gray-scale images) is reminiscent of the late stages of development of the Kelvin-Helmholtz instability (see, for example, Bicknell et al. 1990a). It is therefore of interest to examine the relationship between the Kelvin-Helmholtz instability, the range of jet parameters which are required by the energy budget, and the velocities which are induced in the dense gas through the action of this instability. Since the jet flow envisaged is not highly supersonic, we are justified, for order-of-magnitude purposes, in using growth rates derived from the incompressible Kelvin-Helmholtz instability (Chandrasekhar 1961, p. 481 ff). The growth rate estimated here is faster than the compressible growth rate but the values used are indicative.

For a perturbation $\propto \exp i\omega t$, ω is given by

$$\omega = k_x V_{\rm jet}\left(-\frac{\eta_{\rm jc}}{1+\eta_{\rm jc}} \pm i\,\frac{\eta_{\rm jc}^{1/2}}{1+\eta_{\rm jc}}\right), \qquad (2)$$

where k_x is the x-component of the wavenumber, $\eta_{\rm jc}$ is the ratio of the jet density to the cloud density (as distinct from the ratio of the jet density to the hot ISM density used above). The velocity induced at the surface of the dense material by the instability is $w = \omega \delta z_s$ where δz_s is the deformation of the surface. The other components of velocity add another factor of $2^{1/2}$ so that the amplitude of the total perturbation to the surface velocity is

$$\delta v = 2\pi\sqrt{2}\,\frac{\eta_{\rm jc}^{1/2}}{1+\eta_{\rm jc}}\,\frac{\delta z_s}{\lambda}\,V_{\rm jet} \qquad (3)$$

$$\approx 890 \text{ km s}^{-1}\left(\frac{\eta_{\rm jc}}{10^{-4}}\right)^{1/2}\frac{|\delta z_s|}{\lambda}\left(\frac{V_{\rm jet}}{10^4 \text{ km s}^{-1}}\right), \qquad (4)$$

where λ is the wavelength of the perturbation. Extrapolating this relation to large amplitudes shows that when the instability saturates (when $|\delta z_s| \approx \lambda/2$) the amplitude of the velocity perturbation induced in the dense layer is ~ 450 km s$^{-1}(\eta_{\rm jc}/10^{-4})^{1/2}(V_{\rm jet}/10{,}000$ km s$^{-1})$. If the value of the ratio of jet density to hot ISM density (η) is of the order of unity and the density of the dense cloud is ~ 10 cm^{-3} (see § 4), then $\eta_{\rm jc}$ is $\sim 10^{-4}$, giving an induced velocity amplitude of order 450 km s^{-1}. If $\eta \sim 0.1$ then $\Delta v \sim 140$ km s^{-1}. Thus when the instability develops (on the order of a few growth time scales), regions of the interface collide with a relative velocity $\sim 2\delta v$ and these numerical estimates of δv are consistent with the observed changes of velocity in the knot region of order 200–400 km s^{-1} (Morganti et al. 1991).

2.3.2. *The Instability Time Scale and the Cloud Destruction Time Scale*

The time scale for growth of the instability implied by equation (2) is

$$t_g \approx 3.1 \times 10^5 \text{ yr}\left(\frac{\lambda}{200 \text{ pc}}\right)\left(\frac{V_{\rm jet}}{10^4 \text{ km s}^{-1}}\right)^{-1}\left(\frac{\eta_{\rm jc}}{10^{-4}}\right)^{-1/2}, \qquad (5)$$

© American Astronomical Society • Provided by the NASA Astrophysics Data System

where the fiducial value of λ is given by the actual sizes of the knots. This time scale determines the time over which the velocity perturbations will grow to saturation and develop into shocks. The clouds are destroyed by the shocks on a destruction time scale $t_d \approx \lambda V_{\rm sh}^{-1} \approx \lambda(\Delta v)^{-1}$ which is almost identical to the growth time scale. Unless these time scales are an appreciable fraction of the radio source age, their appearance is transitory and unlikely to be observed. Now Centaurus A in toto is an extremely large source and likely to be quite old. However, the structure of the inner regions of Cen A is quite likely due to a more recent outburst. A rudimentary indication of the relevant time scale for the outburst may be derived from the spectral index variations in the inner northern lobe (Clarke et al. 1992). These indicate ages for the plasma in that lobe of the order of a few $\times 10^6$ yr. For the above instability time scales to be of order this age, one requires jet velocities to be lower than our fiducial value of 10^4 km s^{-1} and/or a value of $\eta_{\rm jc}$, say $\sim 10^{-5}$. In this way, growth and destruction time scales of the order of the estimated age of the inner VLA source can be comfortably achieved and are also consistent with the energy budget.

Of necessity these estimates are only approximate, but they do achieve a measure of consistency with several aspects of the source dynamics. In essence the physical picture is of the development over $\gtrsim 10^6$ yr of supersonic turbulent velocities ~ 200 km s^{-1} through interaction of a dense ($n \sim 10$ cm^{-3}) cloud with a moderate speed ($V \sim 5000$ km s^{-1}) jet. It will be interesting to perform simulations of this envisaged situation. This should confirm some of the physics outlined here and provide more robust estimates of the relevant time scales and velocities.

2.4. *The Hβ Luminosity*

2.4.1. *Equal Density Clouds*

The flow of energy, from kinetic energy of the dense gas to thermal energy in the shocked gas to ionizing radiation to Balmer emission, is relatively straightforward so that order-of-magnitude estimates for the Balmer line intensities are readily derived.

In order to estimate the Hβ luminosity, we consider the collision of two equal density clouds with number density $n \sim 1$ cm^{-3} (Morganti et al. 1991) and relative velocity $\Delta v \sim 200$ km s^{-1}. This is most easily contemplated in the frame in which both clouds have a velocity $0.5\Delta v$ toward each other. In this frame, the end result of the collision is two shock waves traveling with approximately equal velocities into the unshocked plasma. Ideally one could imagine the shocks propagating initially with a speed $\frac{2}{3} \times \Delta v$ with respect to the unshocked material and then decelerating as cooling becomes more important and the shocks lose pressure support. However, the actual situation is more complex. Innes, Giddings, & Falle (1987a, b) and Innes (1992) have shown that if one makes the restriction to one dimension, the shock takes on a pulsating character due to alternating postshock cooling and restoration of pressure support behind the shock. In more than one dimension however, transverse collapse of the thermally unstable postshock plasma is also likely to be important. Therefore, the end result of such a shock is likely to be some variation in shock velocity (of which the Innes et al. and Innes calculations represent an extreme case) accompanied by the formation of numerous filaments and condensations of dense material in the vicinity of the shock. These instabilities all take place on a cooling time scale which (as is shown below) is quite short in the postshock plasma. This structure is pertinent when we consider detailed emission-line modeling in the following sections. For order of magnitude purposes, in this section, we therefore assume that the shock velocity is approximately $0.5\Delta v$.

The temperature behind the shocks produced by the collision is

$$T_{\rm sh} \approx \frac{3}{64}\frac{\mu m_p}{k}(\Delta v)^2 = 1.3 \times 10^5 \left(\frac{\Delta v}{200 \text{ km s}^{-1}}\right)^2 \tag{6}$$

and for $\Delta v \sim 300$–400 km s^{-1} a flux of UV–soft X-ray radiation is produced. Gas yet to enter the shock is photoionized, and the following calculation for an optically thick photoionized region establishes order of magnitude estimates for the emerging Hβ flux as well as scaling relationships for its dependence upon Δv.

The cooling time of the shocked plasma, $t_{\rm cool} = 3kTn_{\rm sh}^{-1}\Lambda^{-1} \approx 4.2 \times 10^{12} T_6 \Lambda_{-22}^{-1} n_{\rm sh}^{-1}$, where $\Lambda \sim 10^{-22}$ ergs cm^{-6} s^{-1} is the usual cooling function. The shocked plasma will expand sideways at approximately the postshock sound speed giving a cooling length $l_{\rm cool} \approx c_s \times t_{\rm cool} \approx 20 T_6^{3/2} \Lambda_{-22}^{-1} n_{\rm sh}^{-1}$ pc. This is considerably less than the dimensions of the knots so that we are justified in assuming that all of the postshock internal energy is radiated as EUV–soft X-ray radiation with a luminosity

$$L = \frac{9}{128} n_0 m_p (\Delta v)^3 A_{\rm sh} = n_{e,\rm sh} n_{p,\rm sh} V_{\rm sh} \int_0^\infty \Lambda_\nu \, d\nu \, , \tag{7}$$

where n_0 is the number density of the unshocked (precursor) region and the subscript sh refers to the shocked region. The monochromatic emissivity of the plasma is represented in the usual way as $n_e n_p \Lambda_\nu(T)$. The number of ionizing photons per second emitted by the shocked material is

$$\mathcal{N} = n_{e,\rm sh} n_{p,\rm sh} V_{\rm sh} \int_{\nu_0}^\infty \frac{\Lambda_\nu}{h\nu} \, d\nu \, . \tag{8}$$

Combining equations (7) and (8),

$$\mathcal{N} = \frac{9}{128 h\nu_0} f n_0 m_p (\Delta v)^3 A_{\rm sh} \tag{9}$$

where the dimensionless parameter is

$$f = \frac{\int_{\nu_0}^\infty (\nu_0/\nu)\Lambda_\nu \, d\nu}{\int_0^\infty \Lambda_\nu \, d\nu} \, . \tag{10}$$

The parameter f depends upon the details of the cooling in the postshock plasma. If one assumes equilibrium cooling (as in Bicknell 1991), the Raymond-Smith (1977) code can be used to give $f \approx 0.3$ over the range of interest. However, the postshock cooling is a nonequilibrium cooling process, where highly ionized species persist longer than in the equilibrium case to give more efficient UV radiation production. The highly ionized species of carbon and oxygen in particular give an enhanced percentage of UV emission in the cooling process as described in Sutherland & Dopita (1993). In the shock models of the following section, a value of $f \approx 0.8$ was achieved.

1993ApJ...414..510S

Standard case B recombination theory (e.g., Osterbrock 1989, Chap. 4) then implies

$$L_{\mathrm{H}\beta} = \frac{9}{128} f \left(\frac{\alpha_{\mathrm{H}\beta}}{\alpha_B}\right)\left(\frac{h\nu_{\mathrm{H}\beta}}{h\nu_0}\right)\left(\frac{\Delta\Omega}{4\pi}\right) n_0\, m_p (\Delta v)^3 A_{\mathrm{sh}}$$

$$= 1.5 \times 10^{36} \text{ ergs s}^{-1} f n_0 \left(\frac{\Delta v}{200 \text{ km s}^{-1}}\right)^3 \left(\frac{A_{\mathrm{sh}}}{10^4 \text{ pc}^2}\right) . \quad (11)$$

This luminosity has a strong dependence upon Δv. However, $\Delta v = 300$ km s^{-1}, $f \approx 0.8$, $n_0 \sim 1$, and $A \approx 4 \times 10^4$ pc^2 gives a value of $L_{\mathrm{H}\beta} \approx 2 \times 10^{37}$ ergs s^{-1}. *This luminosity is consistent within a factor of* 2 *of the luminosities of knots A, B, and C as determined by Morganti et al.* Moreover, the required velocity is within the observed range over a large part of the knot region.

The above calculation implicitly assumes an optically thick pure hydrogen plasma. Naturally, the emission-line luminosity is smaller if the region is optically thin (as we argue in the following section that it is). However, if the optical depth is not too small, equation (11) is still a reasonable order-of-magnitude approximation.

The presence of other ions in the photoionized plasma has a more important effect especially when the ionizing radiation hardens with increasing shock velocity. The fraction of the total field absorbed by the hydrogen cross section is reduced in comparison to other ions which then become more important in the ionization-recombination balance. This has the effect of diminishing the efficiency of Hβ production and the power of Δv in the above equation is reduced. At the same time, the *bolometric* luminosity should maintain an approximate $(\Delta v)^3$ dependence as the input energy emerges in other lines. In detail, the emission from a given line from a complex species such as oxygen is complicated by the ionization balance. The He II ion, with its larger energy range cross section, is more sensitive to the energies of the radiation produced in the $\sim$200–400 km s^{-1} range, without complex ionization balance effects. The He II λ4686 line should therefore display a better $(\Delta v)^3$ dependence than other visible emission lines.

The precise dependence of the Hβ luminosity on Δv is addressed in detail in Sutherland (1993). For the time being we note that despite its shortcomings equation (11) is a useful indicative estimate of the Hβ luminosity to be expected from a given shock velocity.

The substantial increase in emission-line luminosity with higher velocities is consistent with the Morganti et al. observation (1991, 1992) and is a characteristic of these types of shock-induced ionization models. The striking fact about the above calculation is that it gives the correct order of magnitude of the emission-line luminosity relying upon essentially simply physics and observational data.

2.4.2. *Unequal Density Clouds*

As we shall show in the development of this model, it is attractive to consider the collision of clouds of unequal densities. How can these arise in from the surface instability of the interface between the jet and the cloud? One way may simply be to appeal to density variations induced by the hydrodyamic development of the surface instability. Another way, which may be more attractive, is for parts of the surface of the cloud to be heated by the radiation in the shocks to $\sim 10^4$ K. These regions of the surface expand to form low-density clouds, and these collide with the denser parts of the interface. Expansion of gas takes place at a velocity $v_{\mathrm{exp}} = [2/(\gamma - 1)]^{1/2} c_s \approx 26$ km s^{-1} $(T/10^4 \text{ K})^{1/2}$ and the time to expand a distance D is given by $t_{\mathrm{exp}} \approx 3.7 \times 10^6$ yr $(D/100 \text{ pc})$ $(T/10^4)^{-1/2}$. As we show in § 4, the size of the low-density region is possibly less than 100 pc so that this expansion time scale is close to the growth time scale for the instability. Thus the formation of diffuse high-velocity clouds in close proximity to a denser region is quite plausible.

If the colliding clouds are of unequal density, the reflected shocks produced by their collision are of unequal velocities. Following the adiabatic treatment of Landau & Lifshitz (1987), the collision of two clouds produces a contact discontinuity on either side of which are regions of unequal density but equal pressure. (In the nonadiabatic case considered in §§ 3 and 4, this internal region is divided into further zones. However, the general principle discussed here remains the same.) The velocities of the reflected shocks are $v_{\mathrm{sh}} = [(\gamma + 1) p_{\mathrm{sh}}/\rho_{\mathrm{ext}}]^{1/2}$, where p_{sh} is the pressure in the shocked region and ρ_{ext} is the density of gas external to each shock. Clearly then, a density ratio of 10 leads to a shock velocity ratio $\sim$3. Thus a shock proceeding at $\sim$200 km s^{-1} into the less dense gas would be accompanied by a shock traveling at $\sim$60 km s^{-1} in the opposite direction. In this case it is only the fast shock which produces the ionizing radiation which is therefore reduced by a factor of 2. In order to produce the same Hβ luminosity, the product of $n_0(\Delta v)^3$ needs to be increased by approximately a factor of 2 and is therefore not a cause for great concern. Thus within the constraints implied by the data, a single autoionizing shock is adequate. Note that in this case, there are equally important contributions to the Hβ flux from both the low- and high-density regions.

Recently, van Gorkom (1992) has discovered H I gas in the vicinity of the outer filaments with a surface density $\approx 5 \times 10^{20}$ atoms cm^{-3}. This generally supports the notion that the filaments are in fact due to the interaction of dense gas with the radio plasma.

2.5. *Estimate of the Ionization Parameter*

As mentioned earlier, the high excitation of the filaments, as indicated by the value of [O III]/H$\beta \sim 10$ is an important feature of the observations. The main parameter which determines [O III]/Hβ is the ionization parameter

$$Q = \frac{(\text{Number of ionizing photons}) \text{ cm}^{-2} \text{ s}^{-1}}{\text{Atomic number density}} . \quad (12)$$

The physical meaning of Q is that it represents the velocity of an ionization front produced by the field. The contribution to the ionization parameter per fast shock is given by

$$Q_0 = \frac{\mathcal{N}}{n_{\mathrm{ph}} A_{\mathrm{sh}}} \quad (13)$$

$$= \frac{9}{256} (h\nu_0)^{-1} f m_p \frac{n_0}{n_{\mathrm{ph}}} (\Delta v)^3$$

$$= 2.8 \times 10^6 \text{ cm s}^{-1} f \frac{n_0}{n_{\mathrm{ph}}} \left(\frac{\Delta v}{100 \text{ km s}^{-1}}\right)^3 , \quad (14)$$

where n_0 is the density in the diffuse region and n_{ph} is the density in the photoionized region (which may or may not be equal to n_0). For equal (or nearly equal density) shocks, the total ionization parameter $Q = 2Q_0$; for shocks of greatly dif-

© American Astronomical Society • Provided by the NASA Astrophysics Data System

fering density, $Q \approx Q_0$. Generally, a value of $Q \sim 10^8$ cm s^{-1} is required to give a value of [O III]/H$\beta \sim 10$. It can readily be seen from the expression for Q_0 that, in the equal density case with $f \approx 0.8$, $\Delta v \approx 300$ km s^{-1} and $n_0 = n_{\rm ph}$ that Q is indeed of this magnitude. A slight increase in Δv in the unequal density case achieves the same result in the diffuse region. Furthermore, when the photoionized region is, say, an order of magnitude more dense than the diffuse high-velocity region, then the ionization parameter has a more moderate value and the corresponding emission is of lower excitation.

3. PARAMETERS AND STRUCTURE OF THE EMISSION-LINE MODELS

3.1. *Preamble*

In order to justify our ideas for the excitation of these filaments, it is necessary to calculate spectra and to show that these are at least approximately consistent with the observations. There are four major features of the observations that we need to address:

1. The Hβ luminosity. (This has been addressed in an order-of-magnitude manner in the previous section. However, it is incumbent upon detailed models to reproduce this.)
2. The linear dimensions of the prominent knots of emission.
3. The high [O III]/Hβ ratio observed throughout the filaments. It is well known that this is inconsistent with other modes of excitation, e.g., slow radiative shocks or excitation by massive O or OB stars.
4. The relatively high fluxes in a number of low excitation lines such as [O I] λ6300 and [S II] $\lambda\lambda$6716+31.
5. The temperature-sensitive ratio: $I_{4363}/(I_{5007} + I_{4959})$.

The observed spectra (Morganti et al. 1991) of the brightest knots from the inner filaments are summarized here in Table 2. This table gives the mean intensities and indicates the ranges over which they vary for the observed optical lines. The data are derived from the published spectra by taking the most complete spectra from the bright knots A, B, and C. These spectra are the only ones with reasonably reliable [O III] λ4363 fluxes.

TABLE 2

OBSERVED LINE RATIOS: Hβ = 1.0

		Slit 1[a]			Slit 2[b]		
Transition		Max	Avge	Min	Max	Avge	Min
[SII]	λ6717 + 31	2.490	1.968	1.110	1.820	1.470	1.100
[NII]	λ6584	2.680	1.905	1.300	1.900	1.548	1.160
Hα	λ6563	4.920	4.348	3.950	3.900	3.777	3.640
[OI]	λ6300	1.430	0.977	0.630	1.170	0.815	0.510
[OIII]	λ5007	9.010	7.780	6.100	11.490	10.523	8.600
HeII	λ4686	0.320	0.267	0.210	0.400	0.353	0.280
[OIII]	λ4363	0.190	0.150	0.110	0.200	0.140	0.050
[NeIII]	λ3868	1.520	1.185	1.010	1.660	1.410	1.210
[OII]	$\lambda\lambda$3727	7.700	6.312	5.610	6.430	5.102	3.980
Ratios							
	I_{6725} /Hα	0.560	0.450	0.281	0.474	0.389	0.296
	I_{6584} /Hα	0.615	0.437	0.329	0.501	0.409	0.305
	I_{6300} /Hα	0.291	0.222	0.159	0.305	0.215	0.137
	I_{4363} /(I_{5007} + I_{4959})	0.017	0.013	0.010	0.013	0.008	0.004
	I_{5007} /I_{3727}	1.463	1.239	1.000	2.721	1.736	1.337

[a] Slit position toward the center of the knots.

[b] Slit position on edge toward radio jet and nucleus.

Before embarking on a description of the results of our modeling, we describe in this section the basic structure of the models and the parameters which we employ. The model results are described in the following section.

Based on the arguments of the previous section, we discuss a logical sequence of models of increasing complexity, each of which has its own appealing features. We believe that the physical situation envisaged in the third model is probably the most realistic for reasons we describe below. Our model sequence is as follows:

1. The collision of two equal density clouds with either optically thick or thin precursors.
2. The collision of two unequal density clouds with an optically thin precursor on the low-density side. This is modeled using infinite plane parallel geometry.
3. The collision of two unequal density clouds, as above, with allowance for interface instabilities.

(The term "precursor" refers to gas which has not entered the shock.)

3.2. *Models*

3.2.1. *Densities and Velocities*

We consider a number of different models involving collisions between clouds of different density ratio (1:1 and 10:1) and with a range of velocities of the primary shock from 150 to 450 km s^{-1}. As pointed out earlier, the velocity field throughout the filaments is highly turbulent with spatially rapid changes in velocity of the order of 150–400 km s^{-1}, and this range of shock velocities effectively brackets the observations.

Using simple recombination (case B) theory and assuming a volume implied by the knots having a similar depth to their observed breadth, the observed luminosity of $\sim 10^{37}$ ergs s^{-1} over a (200 pc)^3 volume requires a hydrogen number density of order unity. Accordingly we use a fiducial value of $n_1 = 1.0$ cm^{-3}.

Figure 1 illustrates our generic collision model. The double shock structure in the middle produces UV and X-ray radiation from at least one of the shocks, and this photoionizes the two clouds. The resulting spectrum in our model is composed

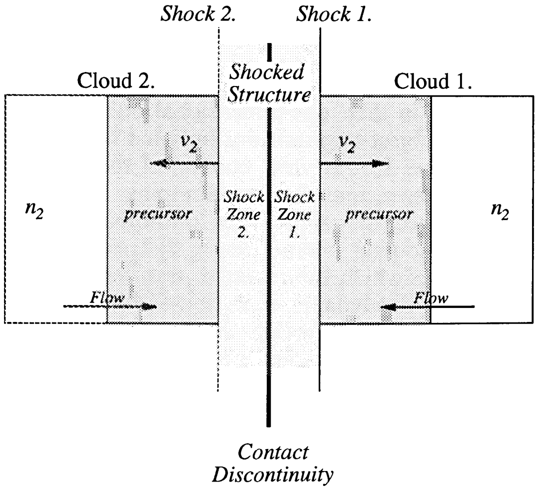

FIG. 1.—Generic cloud-cloud collision model structure. In the collision, a double shock structure forms in the middle, with shocks traveling out from the central contact discontinuity.

© American Astronomical Society • Provided by the NASA Astrophysics Data System

TABLE 3

ABUNDANCES: log NUMBERS RELATIVE TO H = 0.00

H	0.00	C	-3.44	Ne	-3.91	Si	-4.45	Ca	-6.64
He	-1.01	N	-3.95	Mg	-4.42	S	-4.79	Fe	-6.33
		O	-3.07	Al	-5.53	Ar	-5.44	Ni	-7.75

of a contribution from the hot shocked material and the cooler photoionized plasma zones.

In all of the models discussed here, we use an infinite plane-parallel approximation with some modifications to be discussed later.

3.2.2. *Abundances*

In the absence of contrary evidence, we assume solar abundance levels (Anders & Grevesse 1989) for all of the models. The elements included in these calculations and the abundance levels are given in Table 3.

In addition to the normal abundance ratios, the heavy elements Ca, Fe, and Ni were depleted by factors of 10–100 in order to prevent emission from these species from becoming too strong. In particular, the newly implemented Fe II ion calculations in MAPPINGS II, which involve some 353 UV/optical and IR transitions in a 53 level atom model, predict stronger [Fe II] emission than observed unless the iron levels are reduced by a factor of 100 or so. We do not draw any strong conclusions based on these depletions, except to say that they could be consistent with the presence of local dust in the filaments, if the observed steep Hα:Hβ ratio of 3.5–4.5 is due to local reddening. There then remains the question of whether actual depletion by grain adsorption has occurred, but we do not address this problem.

Cross-checks show that the depletions have negligible effect on other lines in the final spectra.

3.2.3. *Allowance for Instabilities*

As we outlined in the previous section, shocks with the velocities which appear to be relevant here are subject to various instabilities whose investigation has only begun in the previously cited papers by Innes and colleagues. Since we do not have a three-dimensional radiation hydrodynamics code, we need to make a number of approximations. In order to appreciate the nature of these approximations, it is best to describe the perfect plane-parallel case first following which we describe our modifications.

The cooling instabilities discussed by Innes (1992) and Innes et al. (1987a, b), in their one-dimensional investigations, produced regions subject to pulsations initiated by the cooling of postshock plasma. In our view, cooling of the postshock gas will, in higher dimensions, lead to clumping, and geometrical effects will reduce the amount of photoionizing radiation absorbed in the cooling stream (see Fig. 2). In reality, determining the degree to which the radiative transfer is affected is a function of the hydrodynamic evolution of the flow. In order to approximate the process within the framework of our one-dimensional treatment, we identify two limiting cases:

1. The flow remains perfectly planar and a one-dimensional treatment for the radiative transfer is adequate.
2. The flow fragments to such an extent that the covering factor of the fragments is quite small and we neglect the absorption of the downstream radiation whilst still following the cooling from this gas.

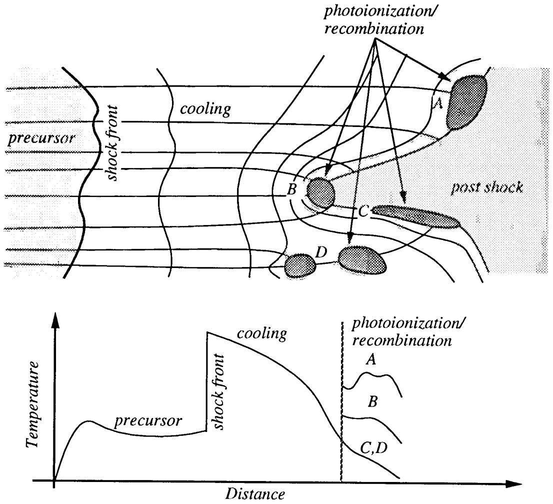

FIG. 2.—Schematic diagram of thermal instabilities in a two-dimensional shocked flow. When the flow fragments due to unstable cooling, the dense cloudlets A, B, C, and D intercept only a small fraction of the downstream field. The amount intercepted by the clouds will produce a range of geometric dilutions of the field.

In the following sections these cases are referred to as the smooth and fragmented cases, respectively.

3.3. *Cloud-Cloud Collision Models*

For the reasons stated above we use a fiducial number density of $n_1 = 1.0 \text{ cm}^{-3}$ for the precursor region. As can be seen from equation (14) in the previous section, the ionization parameter does not depend on density since the energy flux that passes through the shock front is proportional to the density.

Referring to Figure 3 and Table 4, a perfect plane-parallel collision between two variable density clouds has the following structure.

For the equal density case, we have zones A and B only, in a mirror symmetric configuration (case 1 in Fig. 3). The radiation from each shock contributes to both the precursor zones when the central shocked region is optically thin.

The collision of two unequal density clouds is a more complex interaction (case 2 in Fig. 3). A high-velocity shock forms zone B. This high-temperature, collisionally ionized plasma emits strong UV–soft X-ray radiation both upstream of the shock and downstream. The lower density precursor material (zone A) is photoionized by the radiation before it enters the shock. The downstream radiation may form another photoionized zone in the denser cloud (zone C). A secondary shock, with a velocity determined by the primary shock velocity and the cloud-cloud density contrast, is driven into the denser cloud-producing zones D, E, and F. The observed spectrum depends on the contributions from these various zones with their different ionization and density structures. The results section describes the detailed treatment of the zones and the assumptions that have gone into the final computed spectra.

3.3.1. *The Modeling Code, MAPPINGS II*

The modeling carried out here uses a new version of the MAPPINGS code (MAPPINGS II; Sutherland & Dopita

1993ApJ...414..510S

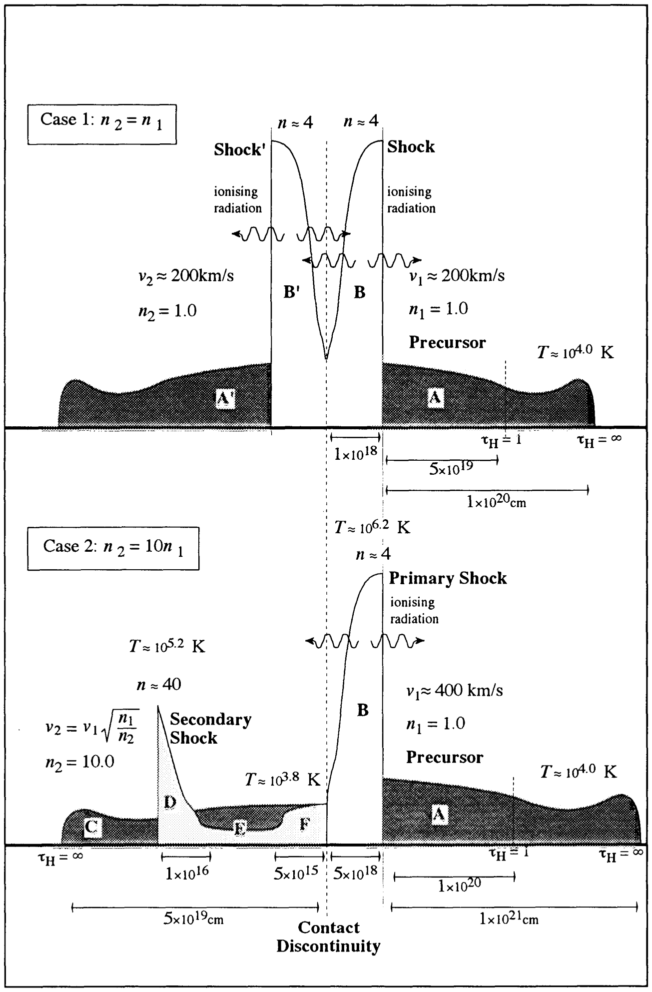

FIG. 3.—Thermal structure of the cloud-cloud collision models. Case 1 represents the case where the two clouds are of equal density and a symmetric structure forms. In case 2, the density contrast between cloud 1 and cloud 2 results in the two shocks having differing velocities and hence different emission properties. See the main text for more details.

1993; Sutherland 1993) which extends the previous version of MAPPINGS (Binette et al. 1985). MAPPINGS II includes atomic data for up to 16 atoms: H, He, C, N, O, Ne, Na, Mg, Al, Si, S, Cl, Ar, Ca, Fe, and Ni. Provision is made for all stages of ionization up to Ni XXIX. However, in the present modeling, only the first 10 or 15 stages are required. Improvements in MAPPINGS II include more rigorous treatment of continuum radiation processes, collisional ionizaton, hydrogenic recombination, and charge exchange reactions. The new code calculates over 1600 resonance, intercombination, and forbidden transitions in the spectral range of Ni XXVIII λ1.24 down to [N II] 205 μm.

The increased ionization range permits the modeling of plasmas up to log $(T) \sim 8$ compared to the log $(T) \sim 5.5$ of the previous version of mappings and far exceeds the old 6 ionization stage limit. This allows us to use one code in a self-consistent way to model collisionally ionized plasma produced by a high-velocity shock together with the detailed interaction of the emitted radiation with the low-temperature photoionization zones associated with the shock.

4. RESULTS

4.1. *Equal Density Cloud Collisions*

We have computed equal density ratio cloud-collision models with the following parameters (see Fig. 3, case 1):

1. Density of precursor (zone A), $n_1 = n_2 = 1$ cm^{-3}.
2. $v_{\text{shock}} = 150, 200, 250$ km s^{-1}.
3. Optical depths (at 911 Å) of precursor region, $\tau_H = 1$, and ∞.
4. Smooth and fragmented shocks.

Two distinct spectra may be formed from the models for each velocity. Both contain the contribution from the photoionized precursor zone A. Where they differ in the postshock zone. In the *fragmented case*, the shocked flow is completely unstable, breaking up into small condensations. In this case the downstream material absorbs none of the downstream radiation field. The dense cooling material radiates a purely cooling spectrum which is not very luminous in Hβ and the low-ionization species are relatively weak in emission. In the *smooth case*, the shocked flow is completely stable and all of the downstream radiation is reabsorbed by the dense downstream material and the center of the shocked structure is optically thick. This produces both very strong low-ionization species and reduces the ionization in the shock precursor zones since the radiation from a given shock cannot reach the opposite shock front.

The results of the equal density models are summarized in Tables 5A and 5B.

Table 5A shows the simplest case where the precursor zone A is optically thick (that is, radiation-bounded). This model implies that the visible knots are just a small fraction of the low-density gas present in the filaments. The spectra produced by the smooth and fragmented cases of this model fail to reproduce the observed spectra. In particular the [O III] λ5007 line is too weak in all of the smooth models and is strong only in the high-velocity fragmented case. When the [O III] emission is strong in the fragmented model, the low-ionization species are too weak (i.e., [O II] $\lambda\lambda$3727). The smooth models produce stronger low-ionization species such as the [S II] lines but fail to produce adequate flux in the high-excitation lines. Thus it is not possible to simultaneously reproduce both the high- and low-ionization species emission with this model.

The optically thin (density-bounded) precursor variants of the equal density models, given in Table 5B, efficiently produce spectra whose high-excitation component is consistent with the observations when the shock velocities are $\sim$200 km s^{-1} or more, and the shocked flow is fragmented. These models imply that the visible knots constitute all of the low-density gas in the filaments.

In the fragmented flow models of Table 5B, strong [O III], [Ne III], and He II lines are produced. The differences from the optically thick models are mainly due to the relatively weaker Hβ emission from the precursor zone. The smooth flow models continue to fail to produce strong [O III] emission even with the relative increase in [O III] emission from the optically thin precursor. This is due to the center of the shock structure becoming optically thick in this case reducing the flux of ionizing radiation into the low-density zone A and enhancing the Balmer and low-ionization emission.

The important temperature sensitive $I_{4363}/(I_{5007} + I_{4959})$ ratio is only in the observed range when the [O III] emission is strong in the 200 km s^{-1} fragmented flow model. At higher

TABLE 4

QUALITATIVE MODEL STRUCTURE

Zone	Temperature (K)	Length (pc)	Density (cm^{-3})	Emission Lines	Notes
A	max 16000	50-1000	n = 1.0 isochoric	Hβ λ5007 λ1909	The main resolved structure. Consists of photoionized low density gas that has not not yet entered the main shock.
B	$1-3\times10^6$	1-10	n = 4 at max T isobaric	λ4363 λλ3737 λ3426 λ1550 λ1240	The hot gas which has passed through the primary shock. Source of the main ionizing radiation field.
C	max 10000	0.5-50	n = 10 isochoric	λ9532 λ5007 λ3869	The part of the denser cloud which is ionized by radiation from the primary shock.
D	$1-5\times10^5$	0.001	n = 40 at max T isobaric	λ6717 λ6584 λ6300 λ4363 λλ3727 λ1548	The slower secondary shock wave which travels into the preionized denser cloud.
E	cold	Variable $\sim(\Delta t\times10^6)$ cm	$n>10^3$ isobaric with B, D and F	Infrared?	Dense gas which cools after having passed through the secondary shock. Not detectable.
F	max 8000	0.001	$n\approx1000$ isobaric	Hβ λ6717 λ6584 λ6300 λλ3727 λ2799	Dense gas which absorbs the radiation field from the primary shock. Extremely bright in a pure planar model. Broken up in a 3D model.

velocities, this ratio drops off below the observed value of $\gtrsim 0.01$ as the contribution from the cooler photoionized zone A increases, and it is too strong when [O III] λ5007 is weak and the contribution from the hot shocked zones become important.

Unfortunately then, for the equal density models, there is only a restricted range of velocities and precursor optical depths possible if both the high-excitation [O III] and [Ne III] lines are to be produced simultaneously with the medium-excitation [O II] lines and a high value of the [O III] λ4363 ratio. Allowing an optically thick center to the colliding clouds increases the low-ionization species at the expense of the high-ionization species since the precursor ionization parameter decreases. In all cases the [O I] lines are too weak.

Thus we may summarize the equal density modeling by stating that these models are attractive in that they correctly reproduce the high-excitation part of the spectrum but indicate that denser cospatial material is required for the low-excitation component. Furthermore, if the equal density cloud model is to explain successfully the majority of the emission using ~200 km s^{-1} models, then thermal instabilities and hence fragmented flows are necessary.

The problems encountered by the equal density model are largely overcome by the unequal density collision models presented in the following subsections which combine the high-radiation fluxes from faster shocks with the efficient production of medium-ionization lines like [O II] λλ3727 from slower shocks produced in the denser material.

4.2. *Unequal Density Cloud Collisions*

We have already, in the previous section, presented an argument as to how different density clouds may arise in the Centaurus A filaments. In this subsection we present models of unequal density cloud collisions with both fragmented and smooth primary shocks (see Fig. 3 and Table 4). In the case of unequal densities, the secondary shock progresses more slowly into the dense material at $v_2 \approx v_1(n_1/n_2)^{1/2}$, where v_1 is the speed of the fast, primary shock and n_1 and n_2 are the corresponding densities (see Fig. 3, case 2).

When we considered the equal density case above, we were able to appeal to instabilities in order to make the central regions optically thin. This is not possible here, for although the tail of the primary shock can be rendered optically thin by fragmentation, zones E and F of the secondary shocked region are always optically thick in pure plane-parallel models. In either case (that is, smooth or fragmented primary shock), the downstream radiation from the primary shock is always absorbed in a very dense ($n\sim10^3$ cm^{-3}) isobaric zone F. The spectra from these two cases are very similar.

In considering the density contrast used in our models, we should note the neutral hydrogen observations of van Gorkom

TABLE 5A

EQUAL DENSITY MODELS, PRECURSOR $\tau_H = \infty$

Transition		150 km s^{-1}		200 km s^{-1}		250 km s^{-1}	
		Smooth	Frag.	Smooth	Frag.	Smooth	Frag.
[SIII]	λ9532	0.467	0.806	0.824	0.997	0.990	0.748
[SII]	λ6717+31	1.473	0.643	1.982	0.315	2.390	0.208
[NII]	λ6584	1.167	1.235	1.169	0.556	1.392	0.416
Hα	λ6563	3.008	2.979	2.961	2.943	2.927	2.904
[OI]	λ6300	0.234	0.061	0.513	0.061	0.809	0.048
[OIII]	λ5007	1.225	1.780	2.758	5.714	5.726	12.121
HeII	λ4686	0.033	0.043	0.045	0.072	0.053	0.088
[OIII]	λ4363	0.065	0.063	0.044	0.051	0.050	0.083
[NeIII]	λ3869	0.135	0.146	0.203	0.320	0.333	0.626
[OII]	λλ3727	3.730	4.000	3.236	2.475	3.098	1.639
[NeV]	λ3426	0.028	0.028	0.142	0.142	0.095	0.109
Ratios							
	I_{6725} /Hα	0.490	0.216	0.669	0.107	0.817	0.072
	I_{6584} /Hα	0.388	0.415	0.395	0.189	0.476	0.143
	I_{6300} /Hα	0.078	0.020	0.173	0.021	0.276	0.017
	$I_{4363}/(I_{5007}+I_{4959})$	0.035	0.023	0.010	0.006	0.006	0.004
	I_{5007}/I_{3727}	0.328	0.445	0.852	2.309	1.848	7.395
Hβ Luminosity[a]		0.42	0.43	0.80	0.81	1.49	1.49

NOTE.—$n_1 = n_2 = 1.0$ cm^{-3}, Hβ = 1.0.
[a] × 10^{37} ergs s^{-1} per (100 pc)^2.

TABLE 5B

EQUAL DENSITY MODELS, PRECURSOR $\tau_H = 1.0$

Transition		150 km s^{-1}		200 km s^{-1}		250 km s^{-1}	
		Smooth	Frag.	Smooth	Frag.	Smooth	Frag.
[SIII]	λ9532	0.336	0.681	0.582	0.734	0.798	0.339
[SII]	λ6717+31	1.783	0.855	2.825	0.702	3.645	0.563
[NII]	λ6584	1.011	0.908	1.282	0.593	1.781	0.460
Hα	λ6563	3.027	3.002	2.971	2.944	2.937	2.894
[OI]	λ6300	0.320	0.125	0.728	0.114	1.222	0.097
[OIII]	λ5007	1.500	3.309	2.122	7.531	3.462	15.379
He II	λ4686	0.046	0.108	0.063	0.206	0.074	0.286
[OIII]	λ4363	0.093	0.155	0.062	0.135	0.060	0.201
[NeIII]	λ3869	0.185	0.333	0.217	0.576	0.270	0.967
[OII]	λλ3727	4.312	6.481	3.849	4.950	4.113	3.846
[NeV]	λ3426	0.040	0.069	0.211	0.420	0.148	0.378
Ratios							
	I_{6725} /Hα	0.589	0.285	0.951	0.238	1.241	0.195
	I_{6584} /Hα	0.334	0.302	0.432	0.201	0.606	0.159
	I_{6300} /Hα	0.106	0.042	0.703	0.039	0.416	0.034
	$I_{4363}/(I_{5007}+I_{4959})$	0.040	0.031	0.053	0.012	0.011	0.009
	I_{5007}/I_{3727}	0.348	0.511	0.198	1.521	0.842	3.999
Hβ Luminosity[a]		0.30	0.17	0.54	0.27	0.96	0.43

NOTE.—$n_1 = n_2 = 1.0$ cm^{-3}, Hβ = 1.0.
[a] × 10^{37} ergs s^{-1} per (100 pc)^2.

(1992) who detected a H I column density of $\sim 5 \times 10^{20}$ cm^{-2}. If the associated cloud were composed completely of H I and were as deep as it is broad, then the hydrogen number density would be approximately 1 cm^{-3}. However, this column density is typical of that for neutral hydrogen with approximately a magnitude of extinction to UV radiation ($A_V \sim 1$) (cf. Kulkarni & Heiles 1988). Therefore, it is more likely that the observed H I represents a surface layer on a more extensive molecular cloud with a density >1 cm^{-3}. This layer would be dissociated by the ambient radiation field (presumably starlight and/or X-rays from the ISM). We therefore use a fiducial value of $n_2 = 10$ cm^{-3} for the dense material in our unequal density collisions. This density is somewhat arbitrary but is large enough to produce qualitatively different spectra from the equal density case. Higher densities present modeling difficulties at present.

Obviously, such a large dense molecular cloud would be the original source of gas which is being ablated by the radio jet to form the observed filaments.

In light of this discussion, we have therefore computed unequal density ratio models which assume plane-parallel homogeneous media, with the following parameters:

1. Density of precursor, $n_1 = 1$ cm^{-3}.
2. Density of secondary cloud, $n_2 = 10$ cm^{-3}.
3. $v_1 = 300$, 400, and 450 km s^{-1}.

© American Astronomical Society • Provided by the NASA Astrophysics Data System

1993ApJ...414..510S

TABLE 6

UNEQUAL DENSITY MODELS, PRECURSOR $\tau_H = 1.0$

Transition		300 km s^{-1}		400 km s^{-1}		450 km s^{-1}	
		Smooth	Frag.	Smooth	Frag.	Smooth	Frag.
[SIII]	λ9532	0.773	0.803	1.178	1.324	1.132	1.267
[SII]	λ6717+31	3.337	3.403	4.163	3.600	4.002	3.335
[NII]	λ6584	1.817	1.889	2.478	2.839	2.480	2.801
Hα	λ6563	2.961	2.962	2.931	2.929	2.930	2.930
[OI]	λ6300	1.173	1.231	1.877	1.643	1.830	1.523
[OIII]	λ5007	3.604	3.608	3.953	4.033	3.236	3.449
HeII	λ4686	0.066	0.065	0.101	0.104	0.098	0.107
[OIII]	λ4363	0.086	0.085	0.099	0.098	0.099	0.103
[NeIII]	λ3869	0.306	0.312	0.374	0.427	0.333	0.408
[OII]	$\lambda\lambda$3727	5.052	5.316	5.345	6.424	5.235	6.368
[NeV]	λ3426	0.080	0.081	0.118	0.120	0.176	0.186
Ratios							
	I_{6725} /Hα	1.127	1.149	1.420	1.229	1.366	1.138
	I_{6584} /Hα	0.614	0.638	0.846	0.969	0.846	0.956
	I_{6300} /Hα	0.396	0.416	0.641	0.561	0.625	0.520
	$I_{4363}/(I_{5007}+I_{4959})$	0.018	0.017	0.018	0.018	0.023	0.022
	I_{5007}/I_{3727}	0.713	0.679	0.740	0.628	0.618	0.542
Hβ Luminosity[a]		2.02	2.09	3.72	3.90	4.95	5.19

NOTE.—$n_2 = 10n_1 = 10.0$ cm, H$\beta = 1.0$.

[a] $\times 10^{37}$ ergs s^{-1} per (100 pc)^2.

4. Optical depth (at 911 Å) of primary precursor region, $\tau_H = 1$.
5. Smooth and fragmented primary shocks.

The computed spectra are composed of a weighted combination of the spectrum from the optically thin main shock precursor (zone A), the main shock itself (zone B), and the secondary shock (zone D). Depending on whether the main shock is smooth or fragmented, there is a contribution from a low-ionization parameter zone in the main shock or the secondary shock tail, respectively (zone F).

When calculating the emission from zone D, we can make some further modeling simplications. The recombination time scale in the unshocked dense cloud is $\sim 10^{13}/n^2 \approx 10^{11}$ s and the cloud destruction time scale (which essentially determines the lifetime of the observed structures) for the primary shock is $\sim 10^{13}$ s. The secondary shock becomes optically thick in $\sim 10^{10}$ s. Thus any region of the dense cloud which is promptly preionized by the primary shock is quickly cut off, and any preionization of this region is completely due to the much weaker field of the secondary shock. This means that we can use an independent, self-consistent model for the secondary shock and calculate its spectral contribution independently. The spectra obtained in this way are summarized in Table 6.

As expected from the results of the equal density models, the optically thick zone in the center of the shocked structure (zone F) produces very strong emission from the low-ionization species such as [S II]. In these models the secondary shocks do produce the required strength of [O II] λ3727 emission, but the emission from [O III] is too weak.

The most encouraging feature of these spectra is the apparent lack of velocity dependence of the line ratios. This is mostly due to the fact that zone F is in a similar density and ionization state for all velocities and is an intrinsically bright component.

In summary, these models produce fairly constant spectra which are of too low excitation. The resolution of this problem lies in accounting for the formation and possible destruction of the low-excitation zone F and is discussed in the following subsection.

4.3. *Unequal Density with Interfacial Instabilities*

In our final model refinement, we modify the model described in the previous section by relaxing the plane-parallel assumption in the region of the contract discontinuity. (This is in addition to the relaxation of this assumption in the primary shock flow.) This is in an attempt to account better for thermal/hydrodynamic processes expected to arise in this type of situation as well as to obtain a closer fit to the observed spectra.

In the pure plane-parallel model, zone F intercepts *all* of the downstream radiation from zone B, regardless of the smooth or fragmented nature of B. If zone A is optically thin ($\tau_H < 1.0$), then zone F is the brightest optical component of the model. The extremely strong emission of [S II] $\lambda\lambda$6717+31 and [N II] λ6584 from this zone overwhelms the red part of the spectrum, and these lines may even exceed the Hα intensity (see Table 6).

In zone F we cannot appeal to thermal instabilities since the secondary shock plasma is not thermally unstable. Nevertheless, additional instabilities at the contact discontinuity can be expected. If the collision is even slightly oblique, shear instabilities will occur. We should also emphasize that in the pure plane-parallel model, zones D, E, and F are extremely thin, of the order of 0.01% the thickness of the entire region. Thus, in the pure plane-parallel approximation we have the somewhat absurd situation of a thin but extremely dense "skin" absorbing most of the radiation from the primary shock. This skin will obviously be broken up by the shear instabilities just mentioned and any turbulent velocity across the interface. Disruption of the thin layers representing zones D, E, and F results in the diminished luminosity of F. The luminosity of F is derived from the reprocessing of the ionizing radiation field, and if it breaks up, then its emission line spectrum fades rapidly. This is due to both the smaller fraction of intercepted radiation and to the resulting lower temperatures. The lower temperature leads to higher densities and a shift toward lower energy, infrared fine-structure transitions as the main cooling. Line quenching at higher densities will eventually limit even these mechanisms. Zone D, on the other hand, is a shock struc-

© American Astronomical Society • Provided by the NASA Astrophysics Data System

ture and is self-luminous. It is not greatly affected by breaking up on scales greater than 10^{16} cm or so.

In contrast to the zone D calculations in Table 6, an effect that follows from the breakup of the dense thin layers in the interface region needs to be taken into account. The main radiation field from the primary shock flows past the secondary shock and preionizes the dense material into which the secondary shock is traveling. This results in a more highly ionized precursor zone for the secondary shocks than is produced in the simple self-consistent shock models used in the previous model. In this model we use the radiation from the primary shock to preionize the dense cloud forming zone C (see Fig. 3, case 2).

This extra preionization occurs when the speed of the ionization front from the primary field exceeds the secondary shock speed, that is when the ionization parameter $Q_2 > v_2$. Using the estimate of Q from the previous section and the above estimate for v_2 shows that when

$$\beta = n_2/n_1 \lesssim 25\left(\frac{v_1}{200 \text{ km s}^{-1}}\right)^4 ,$$

preionization of the dense cloud by the radiation from the main shock will occur. Our value of $\beta = 10$, together with the velocities used here, implies that preionization of D by the primary shock field always occurs.

The final computed spectra are therefore composed of some of the components from the straightforward unequal density models described above in § 4.2. We further assume that interface instabilities break up the thin layers D, E, and F reducing the spectral component of F, and it is removed from the integrated spectrum. There is a new contribution from zone C that is of moderately high ionization, and the secondary shock zone D has a different preionization state. These spectra are combined to give Table 7.

These spectra give a very satisfactory fit to the observations. The ratios do not display a particularly strong velocity dependence within the modeling range of 300–450 km s^{-1}. We also present the spectra as they would appear with some local reddening. Adopting a reddening constant $c = 0.5$ and employing the standard reddening function of Kaler (1976) reproduces the observed Hα-to-Hβ ratio. This generally improves the spectra fit, strengthening the red [S II], [N II], and [O I] lines and not affecting the [O III] lines significantly. The [O II] λλ3727 emission is slightly weaker than the published values of Morganti et al. (1991), but as this line was on the very edge of their detector, these line intensities are subject to the greatest calibration uncertainties.

Any remaining weakness in [O I] λ6300 may possibly be accounted for by zone F persisting to some degree as a very low ionization parameter zone. We have chosen to take a limiting case by simply removing zone F from the spectra, but some spectra with an arbitrarily low ionization parameter could be included to produce strong [O I] λ6300 and very little other optical forbidden line emission.

Overall the global properties of high excitation lines such as [O III], [Ne III] and He II are reproduced. In particular the [O III] $I_{4363}/(I_{5007} + I_{4959})$ ratio is in the observed range. The correct modeling of this ratio has been an outstanding problem with the pure photoionization models, as emphasized by Robinson (1989) and Tadhunter, Robinson, & Morganti (1989). The low excitation lines arise naturally (and strongly) from high density shocked zones, without our having to invoke a wholly arbitrary density distribution a priori.

4.3.1. *The Ionization Gradient*

Projection effects arise since the precursor zone is spatially resolved in the Centaurus A filaments, whereas the shocked structure remains unresolved. A given line of sight might pass through more or less of the precursor zone before reaching the shocked structure. Since the precursor is a strong contributor to the [O III] λ5007 radiation, an [O III]:Hβ gradient could arise with the simple geometry shown in Figure 4. In Table 8 a number of weightings for the spatially resolved and unresolved components are given and these may be compared to the

TABLE 7

BEST MODELS SPECTRA

Transition		Raw Spectra: Velocity (km s^{-1})				Reddened Spectra: c = 0.5 Velocity (km s^{-1})			
		300	350	400	450	300	350	400	450
[SIII]	λ9532	0.663	0.615	0.514	0.374	1.377	1.278	1.069	0.777
[SII]	λ6717+31	1.324	1.539	1.935	2.296	1.994	2.318	2.916	3.460
[NII]	λ6584	1.083	1.080	1.122	1.209	1.592	1.589	1.649	1.777
Hα	λ6562	2.962	2.931	2.922	2.915	4.342	4.295	4.283	4.272
[OI]	λ6300	0.233	0.311	0.459	0.614	0.321	0.430	0.634	0.849
[OIII]	λ5007	8.837	11.499	10.796	9.561	9.169	11.930	11.201	9.920
He II	λ4686	0.170	0.248	0.290	0.270	0.170	0.248	0.290	0.270
[OIII]	λ4363	0.178	0.226	0.243	0.247	0.154	0.195	0.210	0.213
[NeIII]	λ3869	0.678	0.830	0.779	0.681	0.504	0.617	0.578	0.506
[OII]	λλ3727	5.889	5.718	5.490	5.101	4.178	4.057	3.895	3.620
[NeV]	λ3426	0.156	0.198	0.279	0.434	0.101	0.128	0.181	0.281
Ratios									
	I_{6725} /Hα	0.447	0.525	0.662	0.788	0.459	0.540	0.681	0.810
	I_{6584} /Hα	0.366	0.369	0.384	0.415	0.367	0.370	0.385	0.416
	I_{6300} /Hα	0.078	0.106	0.157	0.211	0.074	0.100	0.148	0.199
	$I_{4363}/(I_{5007}+I_{4959})$	0.015	0.015	0.017	0.019	0.012	0.012	0.014	0.016
	I_{5007}/I_{3727}	1.501	2.011	1.967	1.874	2.194	2.941	2.875	2.741
Hβ Luminosity[a]		1.21	1.46	1.96	2.86				

NOTE.—$n_2 = 10n_1 = 10.0$ cm, Hβ = 1.0.

[a] $\times 10^{37}$ ergs s^{-1} per $(100 \text{ pc})^2$.

© American Astronomical Society • Provided by the NASA Astrophysics Data System

1993ApJ...414..510S

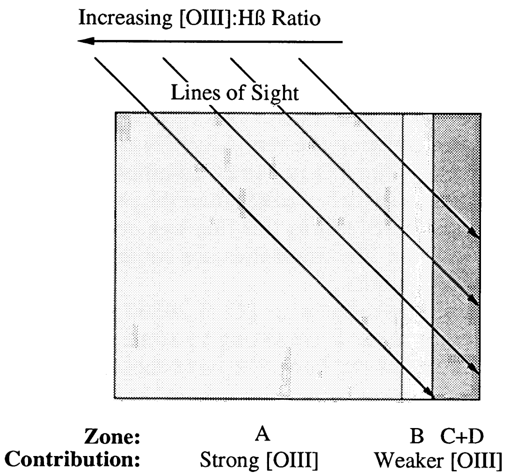

FIG. 4.—The formation of an apparent ionization gradient due to projection effects. [O III] emission will be strongest when the line of sight passes through more of the precursor zone.

TABLE 9A

ULTRAVIOLET SPECTRA: BEST MODELS

Transition		Velocity (km s^{-1}) 300	350	400	450
C I]	λ2967	0.244	0.259	0.268	0.304
Mg II	λ2799	0.546	0.570	0.560	0.537
[Mg V]	λ2783	0.038	0.051	0.059	0.066
C II]	λ2326	1.083	1.046	0.803	0.535
N II]	λ2159	0.104	0.109	0.109	0.089
[Si IX]	λ2149	0.068	0.104	0.095	0.073
C III]	λ1909	2.363	2.504	2.112	1.442
[Mg VI]	λλ1806	0.170	0.164	0.146	0.127
N III]	λ1750	0.349	0.374	0.385	0.329
O III]	λ1666	0.642	0.722	0.783	0.795
HeII	λ1640	1.274	1.860	2.178	2.024
C IV	λλ1549	7.027	14.780	17.168	10.436
N IV]	λ1486	0.143	0.283	0.439	0.478
[Si VIII]	λλ1443	0.304	0.319	0.267	0.205
O IV]	λ1401	0.969	1.453	1.983	2.404
Si IV	λλ1397	1.415	0.874	0.001	0.221
C II	λ1335	4.539	4.323	3.090	1.606
N V	λλ1240	1.089	1.281	2.036	3.705
O V]	λ1218	0.888	0.893	1.080	1.829

NOTE.—$n_2 = 10n_1 = 10.0\ \mathrm{cm}^{-3}$, $\mathrm{H}\beta = 1.0$.

observations of Morganti et al. (1991) (see Table 2) for their slit 1 and slit 2 which are near the knot centers and the edges respectively.

In the [O III] λ5007: Hα ionization gradient map images made by Morganti et al. (1992), it should be noted that the gradients do *not* slope along the line toward the nucleus; rather, in most cases, they point to approximately ~30°–40° counterclockwise to the beam direction in most cases, and in filament A, the ionization gradient is almost perpendicular to the nuclear direction. In our model the projection does not have to lie along the line of sight to the nucleus; we require merely that the general plane of the collision(s) be oblique to our line of sight. In our model we predict that the denser material is generally to the south of the knots, while the jet is passing north of the knots and the general plane of interaction is sloping away from us to the north.

In our interaction model we may further expect a generally higher level of ionization in regions of higher velocity dispersion due to stronger excitation of [O III] by the faster shocks. If a velocity distribution is set up in the cloud-jet interaction with higher velocities nearer to the interaction, then a genuine ionization gradient could also arise. This is especially true in the case of thin equal density cloud collisions which have a stronger [O III] λ5007 velocity dependence (see Table 5B). Indeed the velocity field observations (Morganti et al. 1991; Evans, Morganti, & Ford 1993) do show more velocity dispersion along the edges of filaments where the [O III] radiation is strongest.

TABLE 8

APPARENT IONIZATION GRADIENT

Transition		Unresolved:Resolved 25:75	50:50	75:25
[SIII]	λ9532	0.387	0.514	0.587
[SII]	λ6717+31	1.446	1.935	2.212
[NII]	λ6584	0.840	1.122	1.280
Hα	λ6563	2.891	2.922	2.940
[OI]	λ6300	0.343	0.459	0.524
[OIII]	λ5007	16.043	10.796	7.834
HeII	λ4686	0.410	0.290	0.223
[OIII]	λ4363	0.320	0.243	0.200
[NeIII]	λ3869	1.027	0.779	0.638
[OII]	λλ3727	4.137	5.490	6.253
[NeV]	λ3426	0.439	0.279	0.189

This leads us to the conclusion that the ionization gradient observation does not strongly distinguish between either the beamed nuclear radiation models or the shock autoionization models. However, our shock ionization model does predict the velocity-excitation correlation and allows a more general orientation of the ionization gradient component due to projection effects.

4.3.2. *Predicted UV Spectra*

We present the ultraviolet spectra predicted by the best models, described earlier, in Table 9A. For comparison we also give UV fluxes predicted by Robinson (1992) using a *single slab* photoionization model with a similar power-law photoionizing field to the field used in the Morganti et al. work (see Table 9B). The UV fluxes and line ratios are significantly different in the photoionizations models in comparison with the present shock models. The UV fluxes are relatively weak in the photoionization models. For most of the UV lines, this is essentially a result of the lack of hot shocked plasma providing energetic thermal electrons to collisionally excite the various UV transitions. In the case of C IV λλ1549, there is an additional strong contribution from the secondary shock in our

TABLE 9B

ULTRAVIOLET SPECTRA: BEAMED PHOTOIONIZATION MODELS[a]

Transition		Photo 1	Photo 2
Mg II	λ2799	2.44	2.84
C II]	λ2326	0.76	0.82
C III]	λ1909	0.71	1.14
O III]	λ1666	0.04	0.08
HeII	λ1640	1.76	1.77
C IV	λλ1549	0.09	0.49
O IV]	λ1401	0.01	0.05
C II	λ1335	0.04	0.04

[a] Robinson 1992.

© American Astronomical Society • Provided by the NASA Astrophysics Data System

1993ApJ...414..510S

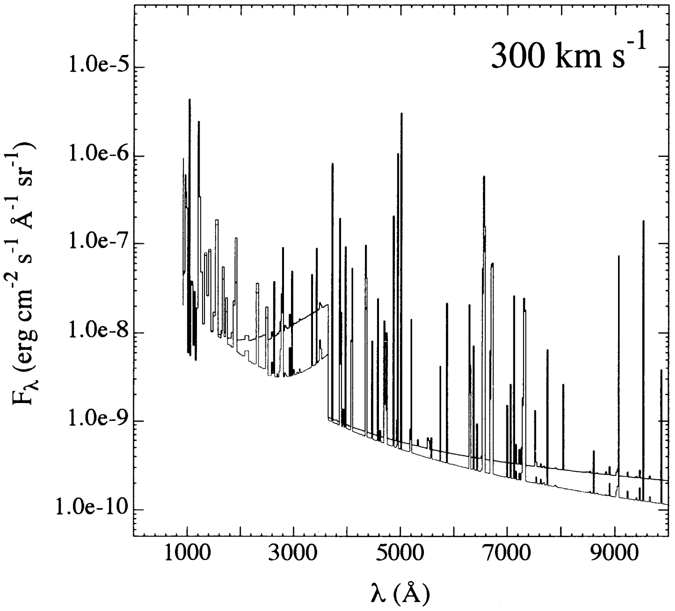

FIG. 5.—Continuum emission for a 300 km s^{-1} model. The gray curve represents the shock contribution, and the solid curve is the total spectrum. The continuum is very weak compared to the line emission.

models (see Table 4). It is possible that a more complex photoionization model involving a spectrum of cloud densities (as used by Morganti et al. 1991) may produce a similar result; however, we feel that it would be difficult for a pure photoionization model to achieve the high temperatures required, as indeed indicated by the low $I_{4363}/(I_{5007} + I_{4959})$ produced by the Morganti et al. models.

We conclude that observations in the spectral region between 3000 Å and Lyman-α may provide a good discriminant between the beaming model and our cloud-cloud collision model.

4.3.3. *Continuum Emission*

The observations do not show any detectable continuum emission. Our modeling is consistent with this. In Figure 5 we present a λ-F_λ plot of the combined emission from a 300 km s^{-1} model. The continuum is obviously weak, and probably unobservable.

The continuum that does exist is dominated by the underlying free-free emission of the fast shock at shorter wavelengths. In the optical the continuum, processes in the photoionization zone make the biggest contribution below the Balmer jump at 3646 Å, but even there the continuum remains very weak compared to the line emission fluxes.

4.3.4. *Energetics and Dimensions*

In Tables 10A and 10B we give the calculated best model dimensions and Hβ luminosities. We give ranges over which the emitting regions may vary in both size and luminosity depending on the optical depths of the photoionized zones. The conversion efficiency of the total primary shock emission to the final total: Hβ luminosity was 173:1 in the 350 km s^{-1} model and similar for the other models. This is quite different to the nominal ratio of 50:1 found in normal H II regions. The conversion efficiency is a complex function of the shock emission spectral energy distribution, the absorbing gas photoionization cross sections, and recombination processes. The final agreement of the Hβ luminosity and velocity of ~300–450 km s^{-1} with the observations is a strong feature of these models. The linear dimensions are also in the observed range.

TABLE 10A

LINEAR DIMENSIONS

	Velocity (km s^{-1})			
	300	350	400	450
Zone **A**, $\tau_H = \infty$	931.132	1928.931	2366.038	3065.409
Zone **A**, $\tau_H = 1.0$	60.157	88.302	104.811	128.270
Zone **B**	1.949	4.157	6.672	9.864
Zone **C**, $\tau_H = \infty$	19.903	32.736	47.673	68.491
Zone **C**, $\tau_H = 1.0$	0.501	0.625	0.836	1.000
Zone **D**	0.001	0.001	0.001	0.001
Zone **F**	0.001	0.002	0.003	0.003
Expected Range*	60-80	90-125	100-160	130-200

NOTE.—$n_2 = 10n_1 = 10.0$ cm^{-3}, Hβ = 1.0. Linear dimensions: parsecs.

* Varying the optical depth of C.

4.3.5. *The Ionizing Radiation*

The ionizing radiation produced by these shock models is the integrated emission from plasmas of a wide range of temperature and nonequilibrium ionization balances. The spectra from the 150, 200, 250, 300, 400, and 450 km s^{-1} models are shown in Figure 6.

The pure photoionization models by Robinson et al. (1987) assumed power law ionizing radiation. Here we show the behavior of the ionizing radiation in our models. The ionizing radiation has a strong dependence on the shock velocity, in both shape and integrated intensity. The spectra produced here are not well approximated by either a blackbody or simple power-law spectrum.

The ionizing spectra are dominated by resonance line emission, especially below ~50 eV. The underlying continuum is a variable component made up of free-bound and two-photon emission at low velocities and becoming dominated, at higher velocities, by free-free emission from a range of temperatures. This results in a brighter and flatter continuum at higher velocities. This changing spectral energy distribution alters the total energy of Hβ conversion efficiency which in turn affects the actual observed dependence of Hβ on Δv (see § 2.4).

The origins of the spectral distributions may be understood in the following terms:

Below ~60 eV the ionizing spectra are all very similar since the major contributions to the spectra are from lower tem-

TABLE 10B

Hβ LUMINOSITIES

	Velocity (km s^{-1})			
	300	350	400	450
Zone **A**, $\tau_H = \infty$	1.10	1.62	2.16	2.50
Zone **A**, $\tau_H = 1.0$	0.24	0.33	0.35	0.44
Zone **B**	0.11	0.13	0.15	0.17
Zone **C**, $\tau_H = \infty$	1.14	1.70	2.32	2.77
Zone **C**, $\tau_H = 1.0$	0.26	0.30	0.39	0.44
Zone **D**	0.60	0.70	1.08	1.81
Zone **F**	1.07	1.59	2.14	2.53
Expected Range*	1.21-2.09	1.46-2.86	1.96-3.90	2.86-5.20

NOTE.—$n_2 = 10n_1 = 10.0$ cm^{-3}, Hβ = 1.0. Hβ luminosities: $\times 10^{37}$ ergs s^{-1} per (100 pc)^2.

* Varying the optical depth of C.

© American Astronomical Society • Provided by the NASA Astrophysics Data System

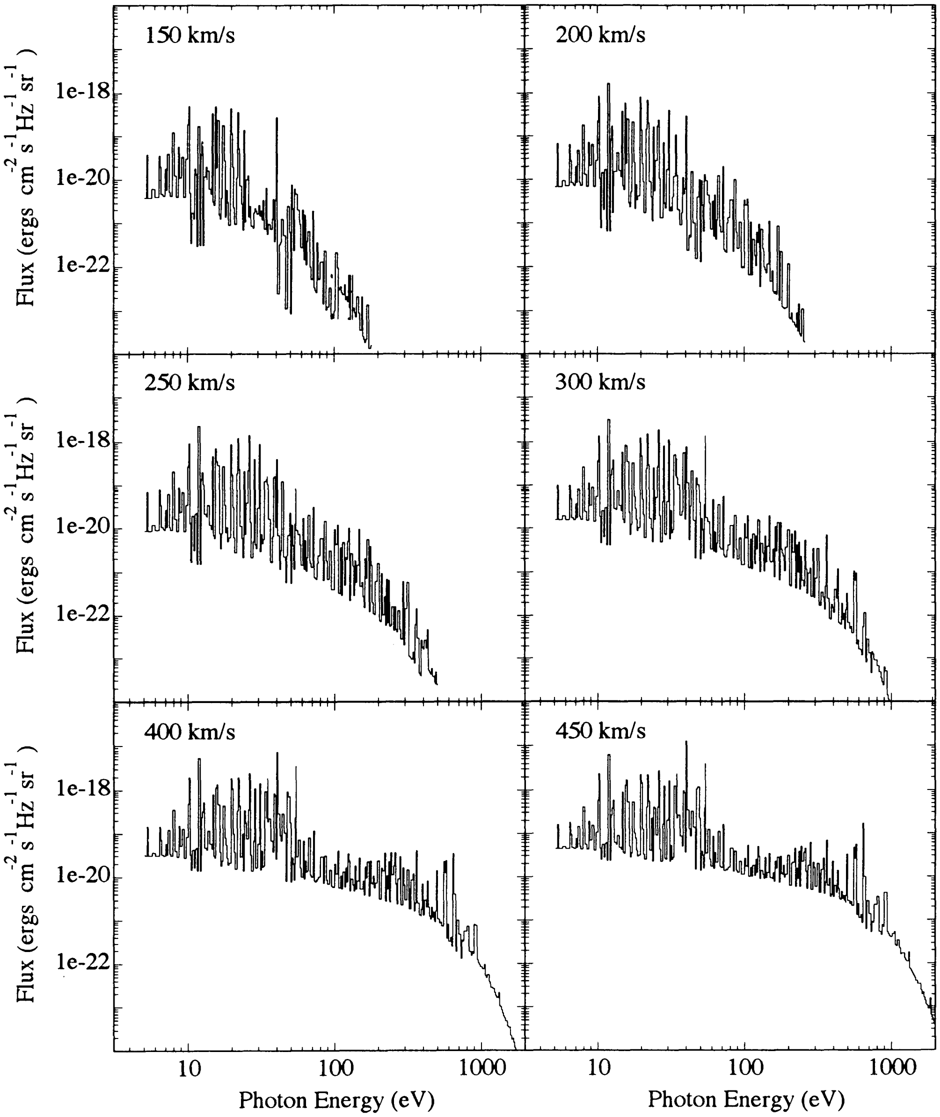

FIG. 6.—The upstream ionizing radiation spectra for fragmented shocks, as a function of velocity

perature plasmas cooling from a similar ionization state following the initial collisional equilibration of the immediate postshock region. This is demonstrated in Figure 7, which shows the oxygen ionization balance for the 300 km s^{-1} fragmented shock model.

After the initial rapid ionization up to O VII (right of A in Fig. 7), there is a long hiatus with the helium-like ion dominating. At the other velocities considered a similar ionization structure occurs because of the inherent stability of the helium like ions. Rapid cooling starts at B due to the increasing populations of very efficient cooling ions like O IV. This cooling process is triggered by the recombination of the highly stripped ions. Since the ionization state always saturates at virtually 100% He like ions of the abundant species (between A and B), the cooling onset, and progress is largely independent of the initial temperature.

Above 60 eV, differences in the spectra occur due to the influence of temperature-dependent continuum processes (such as free-free radiation) in the highest temperature regions of the plasma (i.e., at higher temperatures than B in Fig. 7).

For all shock velocities, the flux of ionizing radiation levels simply increases due to the increasing density of the cooling plasma: Shocks of higher velocity achieve higher pressures, and this translates to a higher density at a given temperature when the plasma cools (see Fig. 6).

5. SUMMARY AND DISCUSSION

In this paper we have presented a model for the emission-line filaments observed along the radio axis of Centaurus A. As we noted in the Introduction, these filaments are of interest not only in their own right but also because of their possible implications for unified schemes of active galaxies and the similarity of their line ratios to other extended and nuclear emission-line regions.

The essence of our model is that shocks, produced through interaction of dense clouds in the environs of Centaurus A with the plasma in the radio jet, emit a sufficient flux of radiation to photoionize the surrounding material. When the shock velocities are more than ~200 km s^{-1}, this gives rise to a charac-

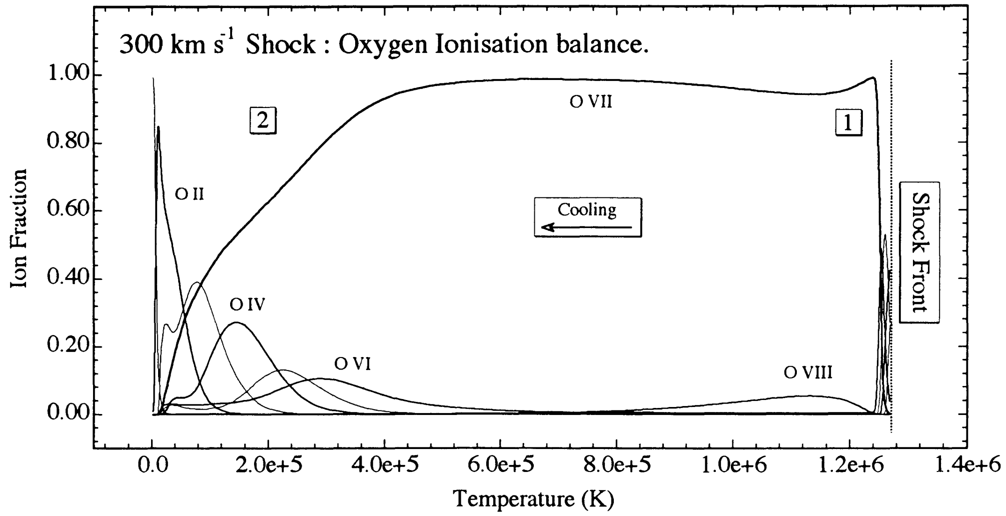

FIG. 7.—Shock model oxygen ionization structure as a function of temperature. Cooling from right to left.

teristically high-excitation spectrum. The observed spectrum is the sum of the high-excitation photoionized zones, the emission from the shock regions, and any high density compressed zones formed in the shock process.

Essentially our model involves a self-consistent treatment of both the dynamics and the emission-line physics of this problem. We have shown that the overall energetics of the knots is consistent with our preconceptions of the densities and velocities of FRI jets. It is also particularly satisfying to see that the turbulent velocities in the knots and their size scale are also consistent with the range of parameters we have assumed for the jet in Centaurus A. Of course, a jet has not yet been detected at the location of the inner filaments and its existence is an important prediction of the model.

The emission-line physics of our cloud-cloud interaction model elucidated in §§ 3 and 4 has only a few free parameters, namely, the initial density, the density contrast, and the shock velocity. The initial density is merely a scaling parameter which is in fact determined from the observations and the shock velocity is also strongly constrained by the observed spectrum. Thus, the only *free* parameter is the density ratio of the two clouds. We have considered two values here, 1:1 and 10:1, since these predict qualitatively different spectra. Some of the 1:1 models are good at producing either low- or high-excitation lines but do not simultaneously produce low-, medium-, and high-excitation lines in the one model. The 10:1 models discussed in § 4.3 satisfactorily reproduce all of the major features of the observed spectra. These include (1) the Hβ luminosity, (2) the sizes of the emission knots, (3) the temperature-sensitive [O III] $I_{4363}/(I_{5007} + I_{4959})$ ratio, (4) the strengths of the high-excitation lines of oxygen, neon, and He II, and (5) the strengths of the low-excitation lines.

The size and luminosities of the regions do not simply follow from the initial estimate in the recombination rate–volume argument given in § 3.2.1. The sizes are affected by the optical depths determined by spectral modeling, and the Hβ luminosities are strongly influenced by the energy conversion efficiency, which is in turn a strong function of the detailed shock cooling/emission process coupled by photoionization and recombination processes in the emitting regions. The fact that the sizes and luminosities are indeed consistent with the observations is an important vindication of this model.

The correct prediction of the temperature-sensitive [O III] ratio is a feature of our model which differentiates it from the alternative beaming model of Morganti and coworkers. Their model requires an additional, unspecified, source of excitation if the [O III] λ4363 intensity is to be explained (Morganti et al. 1991). The reason for the higher value of [O III] λ4363 in our models is that the shock precursor region is significantly hotter than it is in a normal photoionization model and there is also a high-temperature contribution from the shocked regions (zones A and B in Figure 3).

The observed correlation between excitation and velocity dispersion and surface brightness and velocity dispersion is naturally explained by our cloud-cloud interaction model, whereas it would have to be an arbitrary coincidence in the pure beamed photoionization model.

The final picture of the interaction is summarized in Figure 8. The zone labels described in Table 4 and Figure 3 are also used here in this two-dimensional representation. The large low-density zone A is ionized by the radiation from the hot zone B produced by the primary shock traveling into A. The shocked flow in B is fragmented by thermal instabilities, and the contact discontinuity zone is disturbed further by other interface instabilities. The radiation from B penetrates the dense material in D, E, and F to ionize the dense cloud on many ionization fronts C. The secondary shock structure probably exists in the form of multiple secondary shocks (zones D and E). Our final model spectra are a sum of contributions from all these zones.

5.1. *AGN Implications*

Unified theories of active galaxies which invoke beamed radiation and orientation effects to explain the observed population of BL Lac objects, for instance, are appealing from several points of view. This idea has been extended by optical astronomers in order to explain the deficit of observed ionizing radiation from that required to ionize extended emission line regions. Frequently, the "beaming" is due to optical obscuration. However, Morganti et al. (1991) have shown that in the case of Centaurus A, a nuclear photoionizing source is necessarily narrowly beamed, presumably due to relativistic aberration. Nevertheless, the model that we have presented here shows that the beamed energy need not be ionizing radiation

© American Astronomical Society • Provided by the NASA Astrophysics Data System

1993ApJ...414..510S

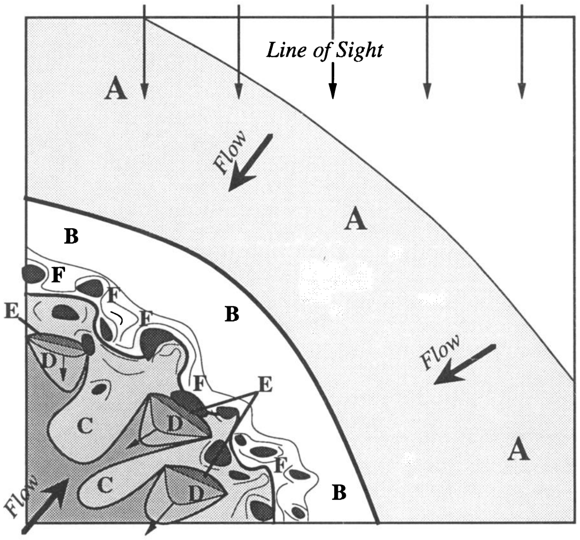

FIG. 8.—Final model schematic structure. See text for details.

but rather a mechanical flux carried by an observable jet. This means that other extended emission-line phenomena may also be energized by a mechanical rather than a radiation process. In even more general terms, our excitation mechanism may apply in any situation where there is bulk turbulent motion of gas with a turbulent velocity ≳200 km s^{-1}. This model may be applied to AGN emission, particularly the narrow-line regions where current models invoke ensembles of moving clouds. Observations of Whittle (1989) show that while some anomalous Seyfert galaxies have [O III] lines with line widths as high as 500–1000 km s^{-1}, the majority have line widths in the range 200–400 km s^{-1}. Our cloud-cloud collision model could be naturally applied to this situation and will again give the characteristic strong forbidden light emission for high- and low-ionization species.

Similarly, Baum (1990) has observed a large sample of emission-line radio galaxies, and interestingly the velocity widths range from 150 to 500 km s^{-1}, raising the prospect that at least some extended emission-line regions are powered by internal shocks. This idea is being currently developed.

5.2. *Conclusions*

We suggest that, for the Centaurus A filaments, our model is to be preferred to the radiation beaming model of Morganti et al. for the following reasons:

As we have stated above, our calculations achieve a high degree of internal consistency in terms of the energy budget, the turbulent velocities observed in the filaments, and the emission-line luminosity, and we are not required to invoke an invisible ionizing beam with an arbitrary beaming factor to explain the data.

The very dense material (zones E and F), which is the source of the lowest excitation lines, is a natural consequence of the physics of the shock waves that we have invoked. In the beaming model, the very dense material is an ad hoc assumption which has to be introduced in order to fit the data.

The pure beaming model is unable to explain the [O III] $I_{4363}/(I_{5007}+I_{4959})$ ratio, and Morganti et al. (1991) are forced to invoke additional heating processes beyond photoionization in order to explain this ratio.

We would like to acknowledge stimulating discussions on this topic with R. Morganti, R. A. E. Fosbury, and I. Evans during the development of the ideas presented here.

One of the authors (R. S. S.) would like to acknowledge the support of an Australian Postgraduate Research Scholarship.

REFERENCES

Anders, E., & Grevesse, N. 1989, Geochim. Cosmochim. Acta, 53(1), 197
Baum, S. A. 1990, ApJS, 74, 389
Bicknell, G. V. 1986, ApJ, 300, 591
———. 1991, Proc. Astron. Soc. Australia, 9, 93
Bicknell, G. V., Cameron, R. A., & Gingold, R. A. 1990a, ApJ, 357, 373
Bicknell, G. V., de Ruiter, H. R., Fanti, R., Morganti, R., & Parma, P. 1990b, ApJ, 354, 98
Binette, L., Dopita, M. A., & Tuohy, I. R. 1985, ApJ, 297, 476
Blanco, V. M., Graham, J. A., Lasker, B. M., & Osmer, P. S. 1975, ApJ, 198, L63
Burns, J. O. 1991, private communication
Burns, J. O., Feigelson, E. D., & Schreier, E. J. 1983, ApJ, 273, 128
Chandrasekhar, S. 1961, Hydrodynamic and Hydromagnetic Stability (Oxford: Clarendon Press)
Clarke, D. A., Bridle, A. H., Burns, J. O., Perley, R. A., & Norman, M. L. 1992, ApJ, 385, 173
Evans, I. N., Morganti, R., & Ford, H. C. 1993, in preparation
Fabian, A. C., Thomas, P. A., Fall, S. M., & White, R. E., III. 1986, MNRAS, 221, 1049
Graham, J. A., & Price, R. M. 1981, ApJ, 247, 813
Innes, D. E. 1992, A&A, 256, 660
Innes, D. E., Giddings, J. R., & Falle, S. A. E. G. 1987a, MNRAS, 226, 67
———. 1987b, MNRAS, 227, 1021
Kaler, J. B. 1976, ApJS, 31, 517
Kulkarni, S. R., & Heiles, C. 1988, in Galactic and Extragalactic Radio Astronomy, ed. G. L. Verschur & K. I. Kellermann (2d ed.; Berlin: Springer-Verlag), Chap. 3
Landau, L. D., & Lifshitz, E. M. 1987, Fluid Mechanics, Vol. 6 (2d. ed.; Oxford: Pergamon Press)
Morganti, R., Fosbury, R. A. E., Hook, R. N., Robinson, A., & Tsvetanov, Z. 1992, MNRAS, 256, 1P
Morganti, R., Robinson, A., Fosbury, R. A. E., di Serego Aligheri, S., Tadhunter, C., & Malin, D. F. 1991, MNRAS, 249, 91
Norman, M. L., Burns, J. O., & Sulkanen, M. 1988, Nature, 335, 146
Osterbrock, D. E. 1989, Astrophysics of Gaseous Nebulae and Active Galactic Nuclei (Mill Valley: Univ. Sci. Books)
Peterson, B. A., Dickens, R. J., & Cannon, R. D. 1975, Proc. Astron. Soc. Australia, 2(6), 366
Raymond, J. C., & Smith, B. W. 1977, ApJS, 35, 419
Robinson, A. 1989, in Extranuclear Activity in Galaxies, ed. E. J. A. Meurs & R. A. E. Fosbury (Garching: ESO), 259
———. 1992, private communication
Robinson, A., Binette, L., Fosbury, R. A. E., & Tadhunter, C. N. 1987, MNRAS, 227, 97
Sutherland, R. S. 1993, ApJS, in press
Sutherland, R. S., & Dopita, M. A. 1993, ApJS, in press
Tadhunter, C. N., Robinson, A., & Morganti, R. 1989, in Extranuclear Activity in Galaxies, ed. E. J. A. Meurs & R. A. E. Fosbury (Garching: ESO), 293
van Bruegel, W. J. M., Miley, G. K, Heckman, T. H., Butcher, H. R., & Bridle, A. H. 1985, ApJ, 290, 496
van Gorkom, J. 1992, private communication
Whittle, M. 1989, in IAU Symp. 134, Active Galactic Nuclei, ed. D. E. Osterbrock & J. S. Miller (Dordrecht: Kluwer), 349

© American Astronomical Society • Provided by the NASA Astrophysics Data System